

## Exclusive electroproduction of $\phi$ mesons at 4.2 GeV

K. Lukashin,<sup>1,2</sup> \* E.S. Smith,<sup>2</sup> G.S. Adams,<sup>28</sup> E. Anciant,<sup>7</sup> M. Anghinolfi,<sup>15</sup> B. Asavapibhop,<sup>20</sup> G. Audit,<sup>7</sup>  
 T. Auger,<sup>7</sup> H. Avakian,<sup>14</sup> J. Ball,<sup>3</sup> S. Barrow,<sup>13</sup> M. Battaglieri,<sup>15</sup> K. Beard,<sup>18</sup> M. Bektasoglu,<sup>25</sup> W. Bertozzi,<sup>21</sup>  
 N. Bianchi,<sup>14</sup> A. Biselli,<sup>28</sup> S. Boiarinov,<sup>17</sup> B.E. Bonner,<sup>29</sup> S. Bouchigny,<sup>2</sup> D. Branford,<sup>11</sup> W.J. Briscoe,<sup>16</sup>  
 W.K. Brooks,<sup>2</sup> V.D. Burkert,<sup>2</sup> J.R. Calarco,<sup>22</sup> D.S. Carman,<sup>24</sup> B. Carnahan,<sup>6</sup> L. Ciciani,<sup>25</sup> R. Clark,<sup>5</sup> P.L. Cole,<sup>32,2</sup>  
 A. Coleman,<sup>34</sup> † D. Cords,<sup>2</sup> P. Corvisiero,<sup>15</sup> D. Crabb,<sup>33</sup> H. Crannell,<sup>6</sup> J. Cummings,<sup>28</sup> P.V. Degtiarenko,<sup>2</sup>  
 L.C. Dennis,<sup>13</sup> E. De Sanctis,<sup>14</sup> R. DeVita,<sup>15</sup> K.S. Dhuga,<sup>16</sup> C. Djalali,<sup>31</sup> G.E. Dodge,<sup>25</sup> J. Domingo,<sup>2</sup>  
 D. Doughty,<sup>8,2</sup> P. Dragovitsch,<sup>13</sup> S. Dytman,<sup>27</sup> M. Eckhause,<sup>34</sup> H. Egiyan,<sup>34</sup> K.S. Egiyan,<sup>35</sup> L. Elouadrhiri,<sup>8,2</sup>  
 A. Empl,<sup>28</sup> R. Fatemi,<sup>33</sup> R.J. Feuerbach,<sup>5</sup> J. Ficenec,<sup>1</sup> K. Fissum,<sup>21</sup> T.A. Forest,<sup>25</sup> A. Freyberger,<sup>2</sup> H. Funsten,<sup>34</sup>  
 S. Gaff,<sup>10</sup> M. Gai,<sup>9</sup> G. Gavalian,<sup>35</sup> ‡ S. Gilad,<sup>21</sup> G. Gilfoyle,<sup>30</sup> K. Giovanetti,<sup>18</sup> P. Girard,<sup>31</sup> K.A. Griffioen,<sup>34</sup>  
 M. Guidal,<sup>26</sup> M. Guillo,<sup>31</sup> V. Gyurjyan,<sup>2</sup> J. Hardie,<sup>8,2</sup> D. Heddl,<sup>8,2</sup> F.W. Hersman,<sup>22</sup> K. Hicks,<sup>24</sup> R.S. Hicks,<sup>20</sup>  
 M. Holtrop,<sup>22</sup> J. Hu,<sup>28</sup> C.E. Hyde-Wright,<sup>25</sup> M.M. Ito,<sup>2</sup> D. Jenkins,<sup>1</sup> K. Joo,<sup>33</sup> § J. Kelley,<sup>10</sup> M. Khandaker,<sup>23</sup>  
 K. Kim,<sup>19</sup> K.Y. Kim,<sup>27</sup> W. Kim,<sup>19</sup> A. Klein,<sup>25</sup> F.J. Klein,<sup>2</sup> \*\* M. Klusman,<sup>28</sup> M. Kossov,<sup>17</sup> L.H. Kramer,<sup>12,2</sup>  
 S.E. Kuhn,<sup>25</sup> J.M. Laget,<sup>7</sup> D. Lawrence,<sup>20</sup> A. Longhi,<sup>6</sup> J.J. Manak,<sup>2</sup> †† C. Marchand,<sup>7</sup> S. McAleer,<sup>13</sup> J. McCarthy,<sup>33</sup>  
 J.W.C. McNabb,<sup>5</sup> B.A. Mecking,<sup>2</sup> M.D. Mestayer,<sup>2</sup> C.A. Meyer,<sup>5</sup> K. Mikhailov,<sup>17</sup> R. Minehart,<sup>33</sup> M. Mirazita,<sup>14</sup>  
 R. Miskimen,<sup>20</sup> V. Muccifora,<sup>14</sup> J. Mueller,<sup>27</sup> G.S. Mutchler,<sup>29</sup> J. Napolitano,<sup>28</sup> S. Nelson,<sup>10</sup> G. Niculescu,<sup>24</sup>  
 I. Niculescu,<sup>16</sup> B.B. Niczyporuk,<sup>2</sup> R.A. Niyazov,<sup>25</sup> A. Opper,<sup>24</sup> G. O’Rielly,<sup>16</sup> J.T. O’Brien,<sup>6</sup> K. Park,<sup>19</sup>  
 K. Paschke,<sup>5</sup> E. Pasyuk,<sup>3</sup> G.A. Peterson,<sup>20</sup> S. Phillips,<sup>16</sup> N. Pivnyuk,<sup>17</sup> D. Pocanic,<sup>33</sup> O. Pogorelko,<sup>17</sup> E. Polli,<sup>14</sup>  
 S. Pozdniakov,<sup>17</sup> B.M. Preedom,<sup>31</sup> J.W. Price,<sup>4</sup> L.M. Qin,<sup>25</sup> B.A. Raue,<sup>12,2</sup> A.R. Reolon,<sup>14</sup> G. Riccardi,<sup>13</sup>  
 G. Ricco,<sup>15</sup> M. Ripani,<sup>15</sup> B.G. Ritchie,<sup>3</sup> F. Ronchetti,<sup>14</sup> P. Rossi,<sup>14</sup> D. Rowntree,<sup>21</sup> P.D. Rubin,<sup>30</sup> F. Sabatié,<sup>25</sup>  
 K. Sabourov,<sup>10</sup> C.W. Salgado,<sup>23,2</sup> V. Sapunenko,<sup>15</sup> R.A. Schumacher,<sup>5</sup> V. Serov,<sup>17</sup> Y.G. Sharabian,<sup>35</sup> § J. Shaw,<sup>20</sup>  
 S. Simionatto,<sup>16</sup> A. Skabelin,<sup>21</sup> L.C. Smith,<sup>33</sup> D.I. Sober,<sup>6</sup> A. Stavinsky,<sup>17</sup> S. Stepanyan,<sup>35</sup> †† P. Stoler,<sup>28</sup>  
 I.I. Strakovsky,<sup>16</sup> M. Taiuti,<sup>15</sup> S. Taylor,<sup>29</sup> D. Tedeschi,<sup>31,2</sup> R. Thompson,<sup>27</sup> M.F. Vineyard,<sup>30</sup> A. Vlassov,<sup>17</sup>  
 K. Wang,<sup>33</sup> H. Weller,<sup>10</sup> L.B. Weinstein,<sup>25</sup> R. Welsh,<sup>34</sup> D.P. Weygand,<sup>2</sup> S. Whisnant,<sup>31</sup> E. Wolin,<sup>2</sup> L. Yanik,<sup>16</sup>  
 A. Yegneswaran,<sup>2</sup> J. Yun,<sup>25</sup> J. Zhao,<sup>21</sup> B. Zhang,<sup>21</sup> Z. Zhou<sup>21</sup> ††

(The CLAS Collaboration)

<sup>1</sup> Virginia Polytechnic Institute and State University, Department of Physics, Blacksburg, VA 24061, USA

<sup>2</sup> Thomas Jefferson National Accelerator Facility, Newport News, VA 23606, USA

<sup>3</sup> Arizona State University, Department of Physics and Astronomy, Tempe, AZ 85287, USA

<sup>4</sup> University of California at Los Angeles, Department of Physics and Astronomy, Los Angeles, CA 90095, USA

<sup>5</sup> Carnegie Mellon University, Department of Physics, Pittsburgh, PA 15213, USA

<sup>6</sup> Catholic University of America, Department of Physics, Washington, DC 20064, USA

<sup>7</sup> CEA Saclay, DAPNIA-SPhN, F91191 Gif-sur-Yvette Cedex, France

<sup>8</sup> Christopher Newport University, Newport News, VA 23606, USA

<sup>9</sup> University of Connecticut, Physics Department, Storrs, CT 06269, USA

<sup>10</sup> Duke University, Physics Department, Durham, NC 27706, USA

<sup>11</sup> Edinburgh University, Department of Physics and Astronomy, Edinburgh EH9 3JZ, United Kingdom

<sup>12</sup> Florida International University, Department of Physics, Miami, FL 33199, USA

<sup>13</sup> Florida State University, Department of Physics, Tallahassee, FL 32306, USA

<sup>14</sup> Istituto Nazionale di Fisica Nucleare, Laboratori Nazionali di Frascati, C.P. 13, 00044 Frascati, Italy

<sup>15</sup> Istituto Nazionale di Fisica Nucleare, Sezione di Genova e Dipartimento di Fisica dell’Università, 16146 Genova, Italy

<sup>16</sup> The George Washington University, Department of Physics, Washington, DC 20052, USA

<sup>17</sup> Institute of Theoretical and Experimental Physics, Moscow, 117259, Russia

<sup>18</sup> James Madison University, Department of Physics, Harrisonburg, VA 22807, USA

<sup>19</sup> Kyungpook National University, Department of Physics, Taegu 702-701, South Korea

<sup>20</sup> University of Massachusetts, Department of Physics, Amherst, MA 01003, USA

<sup>21</sup> M.I.T.-Bates Linear Accelerator, Middleton, MA 01949, USA

<sup>22</sup> University of New Hampshire, Department of Physics, Durham, NH 03824, USA

<sup>23</sup> Norfolk State University, Norfolk, VA 23504, USA

<sup>24</sup> Ohio University, Department of Physics, Athens, OH 45701, USA

<sup>25</sup> Old Dominion University, Department of Physics, Norfolk, VA 23529, USA

<sup>26</sup> Institut de Physique Nucleaire d’Orsay, IN2P3, BP 1, 91406 Orsay, France

<sup>27</sup> University of Pittsburgh, Department of Physics, Pittsburgh, PA 15260, USA

<sup>28</sup> Rensselaer Polytechnic Institute, Department of Physics, Troy, NY 12181, USA

<sup>29</sup> Rice University, T.W. Bonner Nuclear Laboratory, Houston, TX 77005-1892, USA

<sup>30</sup> University of Richmond, Department of Physics, Richmond, VA 23173, USA

<sup>31</sup> University of South Carolina, Department of Physics, Columbia, SC 29208, USA

<sup>32</sup> *University of Texas, Department of Physics, El Paso, TX 79968, USA*  
<sup>33</sup> *University of Virginia, Department of Physics, Charlottesville, VA 22903, USA*  
<sup>34</sup> *College of William and Mary, Department of Physics, Williamsburg, VA 23185, USA*  
<sup>35</sup> *Yerevan Physics Institute, 375036 Yerevan, Armenia*  
(January 16, 2001)

## Abstract

We studied the exclusive reaction  $ep \rightarrow e'p'\phi$  using the  $\phi \rightarrow K^+K^-$  decay mode. The data were collected using a 4.2 GeV incident electron beam and the CLAS detector at Jefferson Lab. Our experiment covers the range in  $Q^2$  from 0.7 to 2.2 GeV<sup>2</sup>, and  $W$  from 2.0 to 2.6 GeV. Taken together with all previous data, we find a consistent picture of  $\phi$  production on the proton. Our measurement shows the expected decrease of the  $t$ -slope with the vector meson formation time  $c\Delta\tau$  below 2 fm. At  $\langle c\Delta\tau \rangle = 0.6$  fm, we measure  $b_\phi = 2.27 \pm 0.42$  GeV<sup>-2</sup>. The cross section dependence on  $W$  as  $W^{0.2 \pm 0.1}$  at  $Q^2 = 1.3$  GeV<sup>2</sup> was determined by comparison with  $\phi$  production at HERA after correcting for threshold effects. This is the same dependence as observed in photoproduction.

PACS number(s): 13.60.Le, 13.60.-r, 12.40.Vv, 14.40.Cs

---

\*Present address: Department of Physics, Catholic University of America, Washington, D.C. 20064.

†Present address: Systems Planning and Analysis, 2000 North Beauregard Street, Suite 400, Alexandria, VA 22311.

‡Present address: Department of Physics, University of New Hampshire, Durham, NH 03824.

§Present address: Thomas Jefferson National Accelerator Facility, Newport News, VA 23606.

\*\*Present address: Department of Physics, Florida International University, Miami, FL 33199.

††Present address: The Motley Fool, Alexandria VA 22314.

‡‡Present address: Department of Physics, Computer Science and Engineering, Christopher Newport University, Newport News, VA 23606.

## I. INTRODUCTION

Vector meson photo- and electroproduction have been important tools used to understand the hadronic properties of the photon [1]. For low values of the four-momentum transfer squared, the photon interacts with the target predominantly through vector meson intermediate states that diffractively scatter off the target. This process, shown in Fig. 1a, was originally described within the framework of the Vector-Meson Dominance (VMD) model. The production of the  $\phi$  meson through this mechanism may be interpreted in terms of the hadronic structure of the photon, that couples to a virtual meson with a strength proportional to the square of the charge of its constituent quarks. Due to the dominant  $s\bar{s}$  quark component in the  $\phi$  meson, quark exchange (e.g. meson-exchange) mechanisms and s-channel resonance production are strongly suppressed [2–5]. As a consequence,  $\phi p$  scattering at low four-momentum transfer proceeds primarily through pomeron exchange, similar to hadron-hadron diffractive scattering.

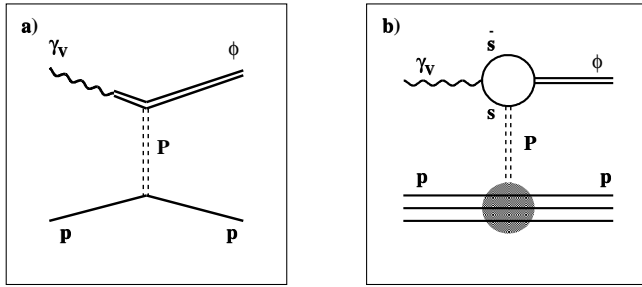


FIG. 1. Representation of  $\phi$  production by: a) the VMD model, and b) the Donnachie and Landshoff pomeron-exchange model.

It is generally believed that the underlying mechanism for pomeron exchange is multi-gluon exchange, where the simplest possibility requires at least two gluons since all hadrons are color singlets. A simplification to these calculations was introduced by Donnachie and Landshoff [6,7], who proposed a model whereby the pomeron couples to quarks inside the interacting hadrons as shown in Fig. 1b. Calculations within this context have been applied to  $\phi$  electroproduction to study the quark substructure of mesons [8,9] and to photoproduction at large momentum transfer [10,11]. In these models the cross section increases slowly with center-of-mass energy,  $W$ , reflecting the pomeron trajectory.

At high  $Q^2$  the pomeron can be resolved into two-gluon exchange, and predictions for hard diffractive electroproduction of vector mesons can be made within the context of perturbative QCD [12]. At lower energies ( $W$

$\lesssim 10$  GeV), quark exchange mechanisms [13,14] become significant for the production of vector mesons with valence  $u$  and  $d$  quarks, but play a limited role in the production of  $\phi$  mesons.

The hadronic structure of the photon arises from fluctuations of the virtual photon into short-lived quark-antiquark ( $q\bar{q}$ ) states of mass  $M_V$  during a formation time [1]

$$\Delta\tau = \frac{2\nu}{(Q^2 + M_V^2)}, \quad (1)$$

where  $-Q^2$  is the squared mass and  $\nu$  is the laboratory-frame energy of the virtual photon (see Appendix A for notation). The effect of the formation time on the propagation of these virtual quantum states in strongly interacting media has been observed for  $\rho$  mesons propagating inside a proton [15] and inside nuclear targets [16]. To date, no clear dependence on the formation time has been observed in  $\phi$  meson production by virtual photons [15,17,18].

This paper presents measurements of exclusive  $\phi$  meson electroproduction off a proton target for  $2.0 \leq W \leq 2.6$  GeV and  $0.7 \leq Q^2 \leq 2.2$  GeV<sup>2</sup> where there is extremely limited data. In this kinematic regime, the short formation distance<sup>1</sup> of the virtual  $q\bar{q}$  state ( $0.35 \leq c\Delta\tau \leq 0.75$  fm) limits the time for interaction and probes the  $\phi$  production mechanism at small formation times.

In Section II we present the details of our experimental techniques and data analysis. It concludes with values for the measured  $t$ -slopes and total cross sections. In Section III we compare our results with previous data, and compare with a geometrical model of the relation between formation time and  $t$ -slope. The model is discussed in some detail in Appendix B.

## II. EXPERIMENT

The experiment was performed using the CEBAF Large Acceptance Spectrometer (CLAS) [19,20] in Hall B of the Thomas Jefferson National Accelerator Facility (Jefferson Lab). The data were taken with a 4.2 GeV electron beam incident on a 5.0 cm liquid hydrogen target in March and April of 1999. The CLAS torus magnet current was set to 2250 A, bending negatively charged particles toward the beam axis. The trigger required

<sup>1</sup>In the literature the formation distance is also referred to as coherence length.

a single scattered electron signal, identified as a coincidence of the forward electromagnetic calorimeter (EC) [21] and Cerenkov counters [22]. Data were recorded at an instantaneous luminosity of  $0.6 \cdot 10^{34} \text{ cm}^{-2} \text{ s}^{-1}$ . This data set has a live-time corrected integrated luminosity  $L_{int} = 1.49 \cdot 10^{39} \text{ cm}^{-2}$ .

**Data Reduction.** In order to reduce the data sample to a manageable size, the data of interest were first pre-selected using very loose requirements on particle identification, missing mass, and the requirement for  $W$  to be above 1.8 GeV. The  $\phi$  mesons were identified through their  $K^+K^-$  decay mode. Because of the small acceptance of  $K^-$  due to the CLAS magnetic field setting, we required only three final-state particles to be detected: electron, proton, and  $K^+$ . The  $K^-$  was reconstructed by identification in the  $epK^+(X)$  missing mass. The momenta of charged tracks were reconstructed from their curvature in the CLAS magnetic field using a system of drift chambers [23]. The data reduction process selected about 82,000 events for further analysis. The size of this filtered data sample was compact ( $\approx 0.5$  GigaByte) and easily manageable in comparison with the size of the entire data set ( $\approx 1$  TeraByte).

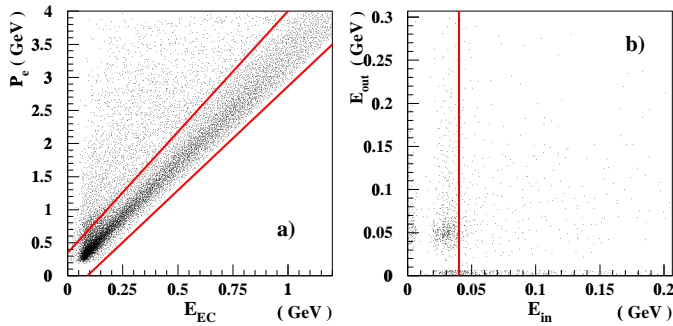


FIG. 2. a) Electron momentum versus total deposited energy in EC. The solid lines show the applied cuts. b) Energy deposited by the TOF-identified  $\pi^-$ 's in the outer EC layers versus energy deposited in the inner EC layers. The solid line shows the applied cut  $E_{in} > 0.04$  GeV, which retains all good electron candidates.

**Electron Identification.** In addition to a fiducial requirement that an electron hit be at least 10 cm from the outer edge of the electromagnetic calorimeter, cuts on energy deposition in the EC were applied in order to avoid misidentification of  $\pi^-$  as  $e^-$ . The total energy deposited by an electron in the EC is proportional to the momentum determined by magnetic analysis. This dependence is illustrated in Fig. 2a. The electron band with the width of the EC resolution is clearly seen. In order to cut out hadronic background, we applied cuts around this band (the solid lines in Fig. 2a). An addi-

tional improvement in  $e^-/\pi^-$  separation was achieved by cutting out the  $\pi^-$  signal based on the energy deposited in the inner layer of the calorimeter as shown in Fig. 2b. The cluster of entries to the left of the line is the  $\pi^-$  signal in the EC. The solid line is the applied cut ( $E_{in} > 0.04$  GeV) to eliminate pions. To determine this cut we used  $\pi^-$  identified by the Time-of-Flight system (TOF) of the CLAS [24].

**Hadron Identification.** The identification of charged hadrons is illustrated in Fig. 3. The distribution of positively charged particle momenta versus reconstructed mass is shown in Fig. 3a. Proton, kaon, and positive pion bands are clearly distinguished. The width of the reconstructed mass increases with momentum. However, there is no systematic dependence after careful timing calibration of the detector [24–26].

**$K^+$  Identification.** In order to optimize the signal-to-background ratio in kaon identification, the kaon momentum range was divided into six bins. In each bin the mass distribution was fitted to a Gaussian with a polynomial background to determine the characteristics of the  $K^+$  peak. An example of this procedure is shown in Figs. 3a-b. The horizontal lines in Fig. 3a show the momentum bins for  $K^+$  identification, and the fitting result for one of the bins is illustrated in Fig. 3b. To identify kaons,  $\pm 2\sigma$  cuts were applied around the mean value ( $m_{K^+}$ ).

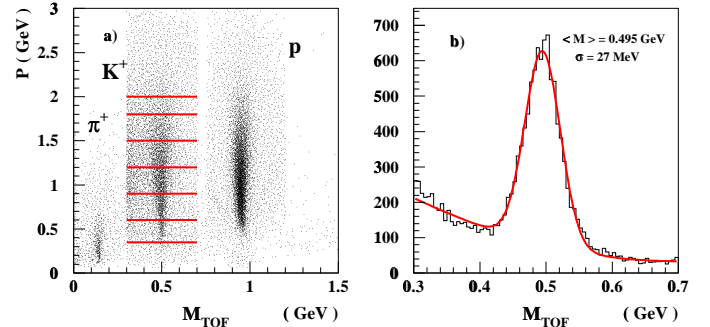


FIG. 3. a) Positively charged particle momentum versus reconstructed mass for the pre-selected event sample. The apparent separation between kaons, pions and protons at high momenta is due to the data pre-selection cuts. The horizontal lines show the binning in kaon momenta; b)  $K^+$  reconstructed mass distribution in the momentum bin from 0.9 to 1.2 GeV. The background is due to pion misidentification.

**Proton Identification.** The proton signal is very clean and does not have a significant background contribution. For proton identification we applied a simple reconstructed mass cut from 0.8 to 1.1 GeV.

**$K^-$  Identification.** We identified the  $K^-$  using the missing mass technique. The  $K^-$  band is clearly seen

in Fig. 4a. The selection used  $\pm 2\sigma$  cuts around the  $K^-$  peak. The invariant mass,  $M_{KK}$ , of the  $K^+K^-$  is computed using the known mass of the kaons, the measured momentum of the  $K^+$  and the missing momentum of the event for the  $K^-$ . We note that because the masses are large compared to the momenta of the particles, this quantity has significantly better resolution than the  $epX$  missing mass.

**Identification of the Signal.** Applying the electron and hadron identification cuts described above, we identified about 3800 events of the  $epK^+K^-$  final state. In order to eliminate events caused by false triggers on low energy electrons (e.g. from  $\pi^0$  Dalitz decays) we also required the energy transfer,  $\nu = E_e - E_{e'}$ , to be smaller than 3.5 GeV. The selected sample includes  $\phi$  mesons, high mass hyperons, and background events that come from particle misidentification.

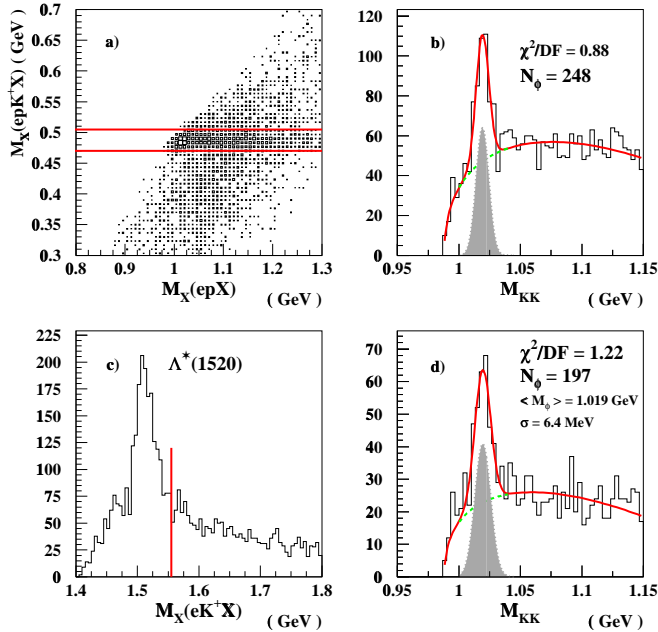


FIG. 4. The  $\phi$  channel separation technique. a)  $epK^+X$  missing mass versus  $epX$  missing mass. The horizontal lines show the selection of  $K^-$ . b)  $M_{KK}$  mass spectrum of  $epK^+K^-$  events. c)  $eK^+X$  missing mass distribution. The line shows the  $\Lambda(1520)$  cut. d)  $M_{KK}$  mass distribution with the  $\Lambda(1520)$  cut applied.

The most important features of the final selection are shown in Figs. 4a-c. In the scatter plot of  $epK^+X$  versus  $epX$  missing mass (see Fig. 4a) the signal of the  $epK^+K^-$  final state is clearly distinguished from the rest of the data. The lines solid show the  $\pm 2\sigma$  selection cuts in the reconstructed  $K^-$  mass. Fig. 4b shows the  $M_{KK}$  mass distribution of the selected final state with a prominent

peak due to exciting  $\phi$  particles. To extract the total  $\phi$  yield, we fitted the peak with a Gaussian (the integral is shown as the filled area in the plot) and the background with an empirical phase space function,

$$f(M_{KK}) = A\sqrt{M_{KK}^2 - M_{th}^2} + B(M_{KK}^2 - M_{th}^2), \quad (2)$$

where the threshold  $M_{th} = 0.987$  GeV. The fit gives  $N_\phi = 248$ , a mean value  $\langle M_{KK} \rangle = 1019.1 \pm 0.6$  MeV, and  $\sigma = 6.0 \pm 0.6$  MeV, where the width of the peak is dominated by the resolution of CLAS.<sup>2</sup> The  $\phi$  signal-to-background ratio is 0.7 within  $\pm 2\sigma$  from the mean value of the  $\phi$  peak.

The primary source of physical background consists of high mass hyperons,  $ep \rightarrow e'K^+Y^*$ , with a subsequent decay  $Y^* \rightarrow N\bar{K}$ . The production and decay amplitudes of these particles are not well known. The main channel is the  $\Lambda(1520)$  with a cross section larger than  $\phi$  production. Additional contributions come from  $\Lambda(1600)$ ,  $\Lambda(1800)$ ,  $\Lambda(1820)$ ,  $\Sigma(1660)$ , and  $\Sigma(1750)$ , which have large branching ratios for decay into the  $N\bar{K}$  channel [27]. These backgrounds were investigated by Monte Carlo using exactly the same algorithms as the experimental data in order to optimize selection cuts. In order to minimize the number of  $\Lambda(1520)$  in the data sample, we require  $M_X(eK^+X)$  to be greater than 1.56 GeV. The cut is shown for the data sample with the solid line in Fig. 4c.

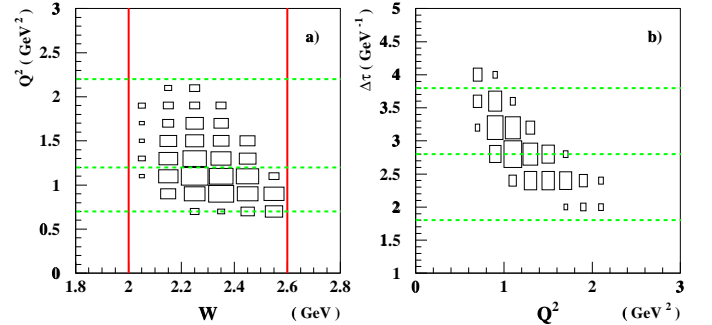


FIG. 5. Kinematic distributions of the selected  $\phi$  events: a)  $Q^2$  versus  $W$ . b)  $\Delta\tau$  versus  $Q^2$ . The dashed lines indicate the binning, used later, in  $Q^2$  and  $\Delta\tau$ ; the solid lines show the range of  $W$  used in the analysis.

The  $M_{KK}$  mass distribution with the  $\Lambda(1520)$  cut applied is shown in Fig. 4d. The simultaneous fit of the  $\phi$  peak and the background gives  $N_\phi = 197$ , a mean value

<sup>2</sup>The mass of the  $\phi$  is  $1019.417 \pm 0.014$  MeV, and the decay width (FWHM) is  $4.458 \pm 0.032$  MeV [27].

$\langle M_{KK} \rangle = 1019.4 \pm 0.9$  MeV, and  $\sigma = 6.4 \pm 1.1$  MeV. The  $\phi$  signal-to-background ratio is improved, and equals 1.3 within  $\pm 2\sigma$  of the  $\phi$  peak. The remaining background, consistent with phase space, is due to high-mass hyperon states, non-resonant  $K^+K^-$  production and experimental misidentification of a  $\pi^+$  as a  $K^+$  (events under the  $K^+$  peak in Fig. 3b). We note that the level of the background under the  $\phi$  peak depends on the fitting procedure, and will be addressed when we discuss systematic errors.

The kinematic range of the data sample is shown in Fig. 5. The range of  $Q^2$  varies from 0.7 to 2.2  $\text{GeV}^2$ ,  $W$  from 2.0 to 2.6 GeV, and  $\Delta\tau$  from 1.8 to 4.0  $\text{GeV}^{-1}$  ( $c\Delta\tau$  from 0.35 to 0.79 fm). The small values of  $c\Delta\tau$  indicate that the formation distance in our kinematic regime is below the hadron size,  $2r_h \approx 2$  fm. The data binning to calculate the exponential  $t$ -slope (see below) is indicated in Fig. 5 by horizontal dashed lines, which show the ranges of  $Q^2$  (integrated over  $\Delta\tau$ ) and  $\Delta\tau$  (integrated over  $Q^2$ ). In both cases the data range in  $W$  is the same (solid lines in Fig. 5a). We note that finer binning in  $Q^2$  and  $W$  is used for the evaluation of the cross sections integrated over  $t'$ .

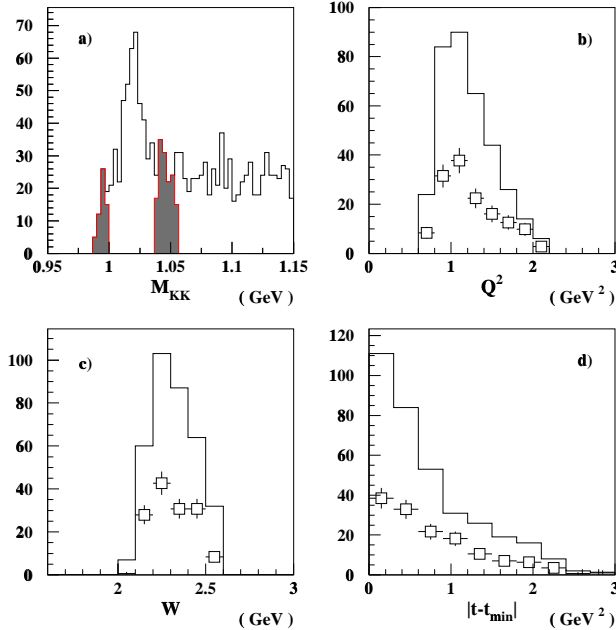


FIG. 6. Side-band background subtraction technique. a) Location of the side bands; b), c) and d) distributions of events in the signal region (histograms) and in the side-bands (open squares) versus  $Q^2$ ,  $W$  and  $|t - t_{min}|$ .

Ideally, with enough statistics and an understanding of the background shape, fits would be used to extract the signal yield in every kinematic bin of interest. With

limited statistics this is not possible, and we proceeded by using a side-band subtraction technique.

**Background Subtraction.** The side-band technique, as illustrated in Fig. 6, was used to determine the background distribution as a function of  $Q^2$ ,  $W$  and  $-t'$ . The signal region was determined within a  $\pm 2\sigma$  cut around  $\langle M_\phi \rangle$  after excluding the  $\Lambda(1520)$  from the final state data sample. The side bands were located  $\pm 3\sigma$  away from the  $\phi$  peak, and the number within the band was scaled to the background as determined by the fit (see Fig. 4d). The normalized side-band events were then subtracted in each distribution of interest. This procedure is illustrated in Fig. 6 for the entire data set and was repeated for each kinematic region defined in Table 1.

Kinematic region	$Q^2$ and $c\Delta\tau$ range	$\langle Q^2 \rangle$ ( $\text{GeV}^2$ )	$\langle c\Delta\tau \rangle$ (fm)	$b_\phi$ ( $\text{GeV}^{-2}$ )
All Data	0.7 – 2.2 $\text{GeV}^2$ 0.35 – 0.75 fm	1.02	0.6	$2.27 \pm 0.42$
Low $Q^2$	0.7 – 1.2 $\text{GeV}^2$	0.87	–	$2.31 \pm 0.59$
High $Q^2$	1.2 – 2.2 $\text{GeV}^2$	1.47	–	$2.10 \pm 0.52$
Low $c\Delta\tau$	0.35 – 0.55 fm	–	0.49	$2.04 \pm 0.42$
High $c\Delta\tau$	0.55 – 0.75 fm	–	0.63	$2.12 \pm 0.46$

TABLE 1. The measured values of the  $t$ -slope parameter,  $b_\phi$ , fitted to the data for  $-t' < 1.2$   $\text{GeV}^2$ . The errors are statistical only.

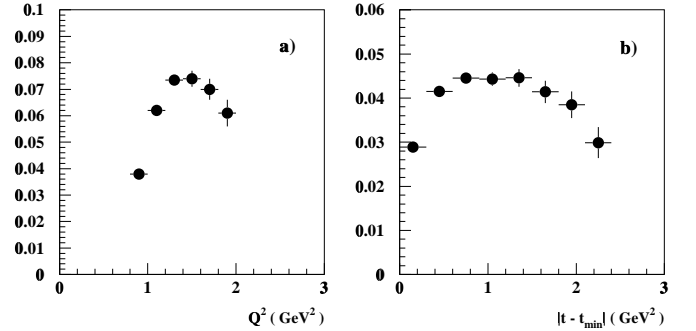


FIG. 7. Acceptance as a function of  $Q^2$  and  $-t'$ .

**Acceptance.** For the calculation of the acceptance, we used a GEANT-based simulation of CLAS, taking into account trigger efficiency, problematic hardware channels, and the CLAS resolution. The Monte Carlo event sample was generated assuming the VMD model for  $\phi$  electroproduction. Two iterations in the acceptance calculation were made to adjust the VMD parameters to be close to the data. In each kinematic region, the acceptance was calculated from the ratio of reconstructed to generated  $\phi$  events with the same kinematics and particle identification cuts that were applied to the

data. Fig. 7 shows the acceptance as a function of  $Q^2$  and  $-t'$  for the entire data set. This procedure was also used to calculate the acceptance as a function of  $W$  and  $\Delta\tau$  in each kinematic bin.

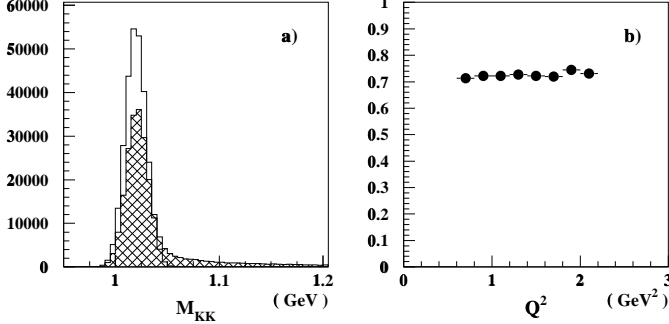


FIG. 8. Simulated data: a)  $\phi$  peak, convoluted with the measured CLAS resolution, with radiative effects turned off (solid), and turned on (hatched histogram). b) Inverse radiative correction factor,  $1/F^{rad}$ , as a function of  $Q^2$ .

**Radiative Corrections.** For the calculation of the radiative corrections, we used the peaking approximation [28]. We define the radiative corrections in each bin of every kinematic variable as the ratio  $F^{rad} = N_{norad}/N_{rad}$ , where  $N_{rad}$  and  $N_{norad}$  are the generated  $\phi$  yields with radiative effects turned on and off, respectively. The model for the  $\phi$  production cross section employed for the computation of acceptance was also used for the studies of radiative corrections. The ratios were calculated with the same kinematics and particle identification cuts that were applied to the data. The simulated  $\phi$  mass distributions with and without radiative effects are shown in Fig. 8a. The inverse radiative correction factor,  $1/F^{rad}$ , as a function of  $Q^2$  is shown in Fig. 8b. The correction factors as a function of  $-t'$  in all four kinematic regions are of the order of 1.4 and uniform over the kinematics considered here.

$Q^2$ bin (GeV <sup>2</sup> )	$\langle W \rangle$ (GeV)	$\langle \epsilon \rangle$	$\Gamma(Q^2, W)$ ( $10^{-4}$ GeV <sup>-3</sup> )	$\sigma(Q^2, W)$ (nb)
0.8 - 1.0	2.37	0.51	$1.50 \pm 0.15$	$27.6 \pm 6.1$
1.0 - 1.2	2.31	0.50	$1.12 \pm 0.10$	$24.2 \pm 5.4$
1.2 - 1.4	2.28	0.49	$0.879 \pm 0.067$	$23.0 \pm 5.2$
1.4 - 1.6	2.28	0.44	$0.701 \pm 0.050$	$20.8 \pm 5.7$
1.6 - 1.8	2.25	0.42	$0.562 \pm 0.033$	$14.5 \pm 6.4$

TABLE 2. The averaged values of  $W$ ,  $\epsilon$ ,  $\Gamma(Q^2, W)$ , and  $\sigma(Q^2, W)$  as a function of  $Q^2$ . The numbers given for the virtual photon flux,  $\Gamma(Q^2, W)$ , computed event-by-event, are the mean and the standard deviation for the bin.

**Data Normalization.** The final step in the analysis procedure was the normalization of the  $\phi$  yield to the

integrated luminosity, the virtual photon flux, and all calculated corrections as:

$$\sigma(Q^2, W) = \frac{N_\phi / BR_{\phi \rightarrow K^+ K^-}}{\Delta Q^2 \Delta W} \frac{F^{acc} F^{rad} F^{win}}{2\pi \Gamma(Q^2, W) L_{int}}, \quad (3)$$

where  $\Delta Q^2$  and  $\Delta W$  are the bin widths in  $Q^2$  and  $W$ ,  $\Gamma(Q^2, W)$  is the virtual photon flux,  $L_{int}$  is the integrated luminosity,  $N_\phi$  is the  $\phi$  yield in the bin,  $F^{acc}$  is the acceptance factor in a given bin,  $F^{win}$  is a small correction factor for production from the target windows ( $\approx 1\%$ ),  $F^{rad}$  is the radiative correction factor, and  $BR = 0.492 \pm 0.007$  is the decay branching ratio for  $\phi \rightarrow K^+ K^-$  [27]. The virtual photon flux was calculated on an event-by-event basis and averaged for each kinematic bin as

$$\Gamma(Q^2, W) = \frac{\alpha}{8\pi^2} \frac{W}{M_p E_e} \frac{W^2 - M_p^2}{M_p Q^2} \frac{1}{1 - \epsilon}, \quad (4)$$

where  $M_p$  is the mass of the proton,  $E_e$  is the electron beam energy, and  $\epsilon$  is the polarization of the virtual photon:

$$\epsilon = \frac{4E_e(E_e - \nu) - Q^2}{4E_e(E_e - \nu) + 2\nu^2 + Q^2}. \quad (5)$$

**Cross Section,  $\sigma(Q^2, W)$ .** The cross section integrated over all  $t'$ ,  $\sigma(Q^2, W)$ , was extracted in five bins over a  $Q^2$  range from 0.8 to 1.8 GeV<sup>2</sup> with a bin width of 0.2 GeV<sup>2</sup>. The range in  $W$  was determined as the allowed kinematic range for each  $Q^2$ . The binning, values of the virtual photon flux used during normalization,  $\Gamma(Q^2, W)$ , and the measured cross section are given in Table 2. The table shows statistical errors only.

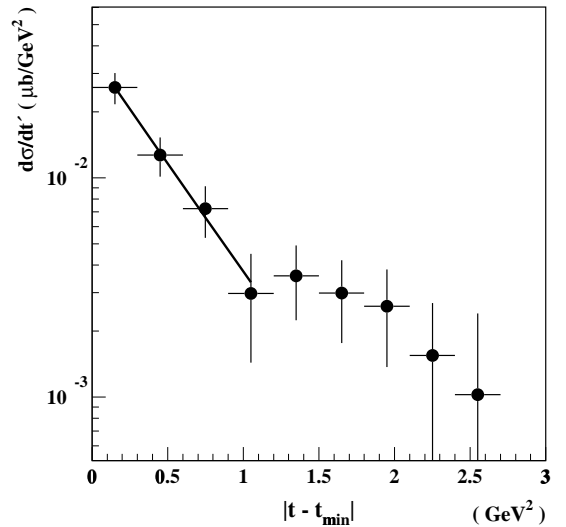


FIG. 9. The  $d\sigma/dt'$  differential cross section for exclusive  $\phi$  electroproduction off the proton.

**Differential Cross Section,  $d\sigma/dt'$ .** The measured cross section,  $d\sigma/dt'$  is generally parameterized at small  $-t'$  by

$$\frac{d\sigma}{dt'} = A_\phi e^{b_\phi t'}. \quad (6)$$

The slope parameter  $b_\phi$  was determined by fitting the data for  $-t'$  less than  $1.2 \text{ GeV}^2$  to compare to previous measurements. Fits were performed in the five overlapping kinematic regions specified in Table 1: the entire data set (plotted in Fig. 9), two ranges in  $Q^2$  (integrated over  $c\Delta\tau$ ), and two ranges in  $c\Delta\tau$  (integrated over  $Q^2$ ). The results of the fit are shown in Table 1. The fit for the entire data set is overlaid on the data in Fig. 9.

At larger  $-t'$ , the slope of the distribution decreases, with an apparent break at  $-t' \approx 1.3 \text{ GeV}^2$ . Therefore, the data suggest that additional mechanisms may be present at  $-t' \geq 1 \text{ GeV}^2$ . A similar pattern is observed in hadron-hadron elastic scattering [29,30], where a dip is observed at  $-t \approx 1.4 \text{ GeV}^2$  followed by a second maximum at  $-t \approx 1.8 \text{ GeV}^2$ . However,  $\phi$  photo-production data do not show a change in the slope for  $-t \leq 2 \text{ GeV}^2$  [11].  $S$ -channel production of resonances results in a large measured value of  $-t'$ . However, there are no known resonances that decay into  $\phi N$ . Finally, imperfect background subtraction could also lead to an enhancement at large  $-t'$ , but should be subsumed into our quoted systematic errors. If we fit the entire range ( $0 \leq -t' \leq 2.6 \text{ GeV}^2$ ) to a single exponential we obtain  $b_\phi = 1.61 \pm 0.31 \text{ GeV}^{-2}$  with a  $\chi^2 = 0.9/\text{DF}$ , which implies that the break is not statistically significant.

Source	$\Delta\sigma(\%)$	$\Delta b_\phi(\%)$
Target stability	0.7	–
Target walls	1.0	–
Acceptance	7.8	5.0
Radiative corrections	4.7	–
Background subtraction	5.4	4.6
Total	10.7	6.8

TABLE 3. Summary of the contributions to the systematic errors.

**Systematic Errors.** Estimates of our systematic errors for the cross section,  $\Delta\sigma$ , and the  $t$ -slope parameter,  $\Delta b_\phi$ , are given in Table 3. The errors are averaged over the kinematics of the experiment, although the lowest  $Q^2$  cross section point may have about twice this systematic uncertainty due to the steepness of the acceptance function (see Fig. 7a). To estimate the systematic errors due to background subtraction, a complete analysis of the cross section and  $t$ -slope parameter was performed using two different assumptions for the shape of the back-

ground: phase space and a constant. The difference between these results is quoted as the systematic error due to background subtraction. The systematic errors due to acceptance and radiative corrections are discussed in Ref. [31] and [32], respectively. Additional details can be found in Ref. [25]. We note that the overall uncertainty is dominated by statistical errors.

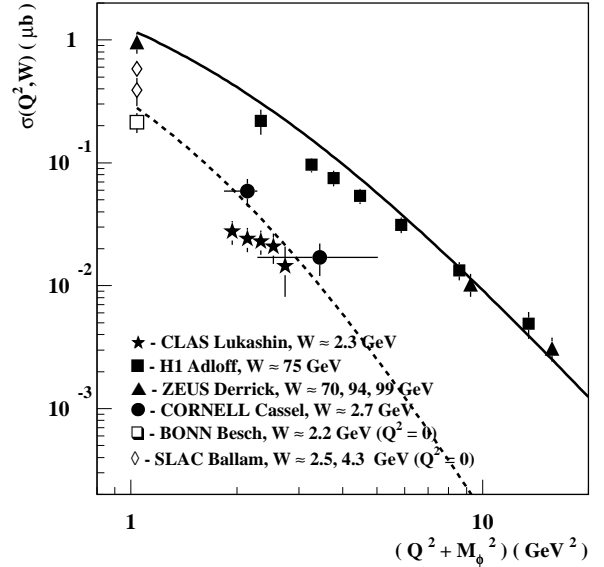


FIG. 10. The  $\phi$  meson cross section dependence on  $Q^2$  for photo- and electroproduction. Electroproduction data H1 Adloff are from Ref. [34], ZEUS Derrick from Ref. [35,36], and CORNELL Cassel from Ref. [15]. Photoproduction data BONN Besch are from Ref. [37], and SLAC Ballam from Ref. [38]. The solid and dashed curves are the pomeron-exchange model predictions for  $W=70 \text{ GeV}$  and for  $2.0 < W < 2.6 \text{ GeV}$ , respectively [10].

### III. RESULTS

**Cross Section Dependence on  $Q^2$  and  $W$ .** The world data on elastic virtual photon production of  $\phi$  mesons are shown as a function of  $Q^2$  in Fig. 10, and as a function of  $W$  in Fig. 11. Selected photoproduction data are also plotted for completeness.<sup>3</sup> We show the data on both plots with common symbols.

All HERA data [34–36] correspond to  $W$  ranging from 40 to 130 GeV, where the gluonic density in the proton at

<sup>3</sup>Additional data of  $\phi$  production on nuclear targets [33] are available at  $\langle W \rangle \approx 14 \text{ GeV}$ .

low  $x = Q^2/2M_p\nu$  plays a significant role. Only the Cornell measurement [15] exists at low  $W$ , corresponding to  $x$  in the valence region.<sup>4</sup> For the high-energy data, the  $Q^2$  behavior of the cross section is well described by the vector meson propagator squared. The data are not yet in the asymptotic perturbative QCD regime where the longitudinal cross section for vector meson production is dominant, and should scale as  $Q^{-6}$  [39]. Nevertheless, the longitudinal contribution becomes increasingly important and must be treated systematically. For example,  $\rho$  mesons in muoproduction at large  $Q^2$  are found to be dominantly in the helicity zero spin state [40].

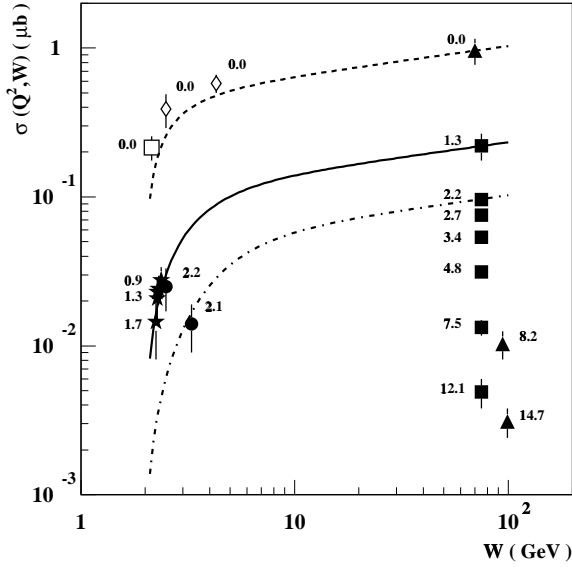


FIG. 11. The  $\phi$  meson cross section dependence on  $W$  for photo- and electroproduction. The  $Q^2$  values of the measurements are printed near the corresponding data points. All data points are from the same References as in Fig. 10. The curves, described in the text, correspond to  $Q^2$  of 0, 1.3 and 2.2  $\text{GeV}^2$ .

Pomeron-exchange models, such as those described in the introduction, reproduce the  $Q^{-4}$  behavior of the data at large  $Q^2$ . The predictions of a model [10], based on the Donnachie-Landshoff pomeron exchange (Fig. 1b), are shown in Fig. 10 for the  $W$  range of our experiment ( $2.0 < W < 2.6$  GeV) and at  $W=70$  GeV. The model describes the data reasonably well at high  $W$ , and reproduces the trend at low  $W$ , but overestimates the new

cross section results presented here. We note that our data are close to the  $\phi$  production threshold, where the cross section increases rapidly as a function of center-of-mass energy. In the model of Pichowsky [8], the transition from a cross section that slowly decreases with  $Q^2$  to one that falls off as  $Q^{-4}$  occurs at a threshold that increases with the current-quark mass of the vector meson. No clear threshold is visible in the  $\phi$  data, but the scarcity of points precludes drawing conclusions.

The photoproduction cross section increases slowly with  $W$ , reflecting the pomeron trajectory. At higher  $Q^2$ , a stronger dependence on  $W$  has been observed in preliminary analysis of HERA data [41]. If the cross section is parameterized as  $W^\delta$ ,  $\delta$  varies from about 0.2 for photoproduction to  $\delta \sim 0.7$  at a  $Q^2$  of 8  $\text{GeV}^2$ . This increased dependence of the cross section on  $W$  has been interpreted as being due to the rise of the gluon momentum density in the proton at small  $x$  [39].

To be able to extract the  $W$  dependence by comparing our measurement at  $Q^2 = 1.3$   $\text{GeV}^2$  to HERA data at the same  $Q^2$  and  $\langle W \rangle = 75$  GeV, threshold effects must be taken into account. For example, threshold behavior can be clearly seen in the photoproduction data [42] (see Fig. 11). The reduced phase space near threshold behaves as  $(\vec{p}_\phi/\vec{q})^2$ , where  $\vec{p}_\phi$  and  $\vec{q}$  are the center-of-mass three-momenta of the  $\phi$  and virtual photon, respectively. This dependence of the cross section on  $W$  can be parameterized as

$$\sigma(W) = \sigma_\circ \left( \frac{\vec{p}_\phi}{\vec{q}} \right)^2 \left( \frac{W}{W_\circ} \right)^\delta. \quad (7)$$

Correcting for the threshold factor, our measurement of the cross section becomes  $\sigma_{corr}(Q^2 = 1.3) = 110 \pm 27$  nb, and using the HERA measurement,  $\sigma(Q^2 = 1.3) = 220 \pm 51$  nb [34], we obtain  $\delta = 0.2 \pm 0.1$ . The quoted uncertainties were obtained by summing the statistical and systematic errors in quadrature. This slope is consistent with that measured in photoproduction. The curves of  $\sigma(W)$  are shown in Fig. 11 for  $Q^2$  of 0, 1.3 and 2.2  $\text{GeV}^2$ , and  $\delta = 0.2$ . The curves are normalized to the HERA data ( $\sigma_\circ, W_\circ$ ) that are far from the production threshold.

**Dependence of  $t$ -slope on  $c\Delta\tau$ .** The dependence of the  $t$ -slope,  $b_\phi$ , on formation distance,  $c\Delta\tau$ , for  $\phi$  meson production is shown in Fig. 12 together with previous data. In the terminology of the uncertainty principle,  $\Delta\tau$  is the time during which the virtual photon, with mass  $\sqrt{Q^2}$ , can fluctuate into a  $\phi$  meson [1]. We expect that  $b_\phi$  should decrease at low  $\Delta\tau$  as the interaction becomes more point-like. The previous electroproduction measurements [15,17,18] do not show the expected behavior. However, a consistent picture emerges when we include photoproduction data as well. Both of our data

<sup>4</sup>We note that data points from Ref. [15] have different integration ranges for the cross section as a function of  $Q^2$  and  $W$  presented in Fig. 10 and Fig. 11.

points (solid stars) lie in the region of  $c\Delta\tau$  below 1 fm, and show a decrease of  $b_\phi$  with decreasing formation time when combined with other data. This is consistent with the well-measured dependence for  $\rho$  meson production [15] as discussed in Appendix B. To fit the  $\phi$  meson data to Eq. B5, we constrain the parameter  $r_h$  to the value extracted from the fit to the  $\rho$  data (Eq. B6). This yields

$$b_\phi(c\Delta\tau) = (6.87 \pm 0.17) \left[ 1 - e^{-c\Delta\tau/2(0.78)} \right] \quad (8)$$

with  $\chi^2/DF = 4.8$ . The fit to the  $\phi$  data is shown in Fig. 12 with the solid curve. The ratio of  $b_\phi/b_\rho$  indicates that the  $\phi$  meson interaction size,  $R_\phi^{int}$ , is smaller than that for the  $\rho$  meson:

$$\frac{b_\phi}{b_\rho} = \left( \frac{R_\phi^{int}}{R_\rho^{int}} \right)^2 = 0.87 \pm 0.08. \quad (9)$$

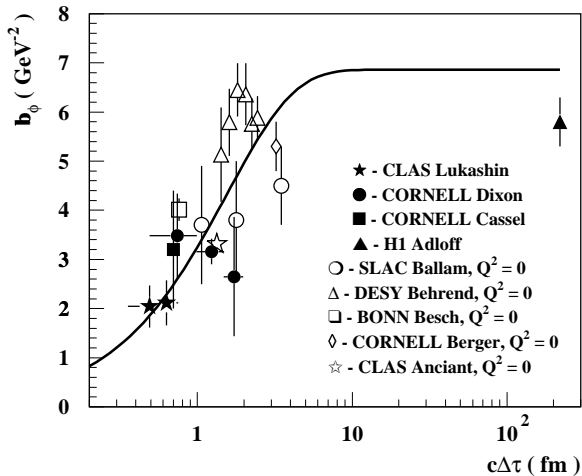


FIG. 12. The dependence of the  $t$ -slope,  $b_\phi$ , on  $c\Delta\tau$ . The electroproduction data CORNELL Dixon are from Ref. [17,18], CORNELL Cassel from Ref. [15], and H1 Adloff from Ref. [34]. The photoproduction data BONN Besch are from Ref. [37], SLAC Ballam from Ref. [38], DESY Behrend from Ref. [42], and CLAS Anciant from Ref. [11].

A summary of the existing measurements of  $b_\phi$  together with our results is shown in Fig. 13. Previous  $\phi$  electroproduction measurements are consistent with no  $Q^2$  or  $c\Delta\tau$  dependence [15,18]. We observe a low value of  $b_\phi \approx 2.2 \text{ GeV}^{-2}$ , which, taken together with the values measured in photoproduction, shows a significant dependence on  $Q^2$ . However, the  $Q^2$  dependence of  $b_\phi$  can be explained by the implicit dependence of  $c\Delta\tau$  on  $Q^2$  (Eq. B7). This is shown in Fig. 13 where we plot the dependence of  $b_\phi$  on  $Q^2$  using Eq. 8 and the relation in Eq. B7 at two values of  $W$ . The lower curve, at  $W = 2.3$

GeV, corresponds to our kinematics and connects our measurements with photoproduction values. The upper curve is closer to the Cornell kinematics.

Because the value of  $c\Delta\tau$  is smaller than the size of the nucleon, the scattering may be considered to be point-like. The application of QCD-inspired models, sensitive to the quark structure of the interacting meson and nucleon, should provide an interesting interpretation of the observed  $b(\Delta\tau)$  and  $b(Q^2)$  dependencies. It has been argued that with increasing  $Q^2$  the radius of the virtual vector meson will shrink [1], and a corresponding decrease of  $b$  should be observed. At large enough  $Q^2$ , quark models [43,44] predict the decrease of the transverse dimension of the vector meson as  $r_V \sim r_h M / \sqrt{M^2 + Q^2}$ . The mass scale  $M$  represents a typical hadronic mass scale, which might be as small as the vector meson mass, e.g.  $M_\phi = 1020 \text{ MeV}$ , but is likely to be large compared to the  $Q^2$  values of this experiment. Even though we do not need to invoke an explicit  $Q^2$  dependence to describe our data, we note that the effects of transverse size and fluctuation times are not easily separated, especially when fine binning is prohibitive due to limited statistics.

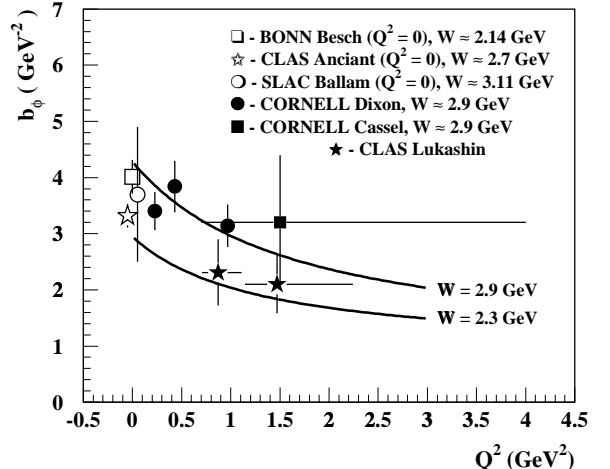


FIG. 13. The dependence of the  $t$ -slope,  $b_\phi$ , on  $Q^2$ . Photoproduction data BONN Besch are from Ref. [37], SLAC Ballam from Ref. [38], and CLAS Anciant from Ref. [11]. Electroproduction data CORNELL Dixon are from Ref. [17,18] and CORNELL Cassel from Ref. [15].

#### IV. SUMMARY

The electroproduction of the  $\phi(1020)$  vector meson was measured for  $Q^2$  from 0.7 to 2.2  $\text{GeV}^2$ ,  $W$  from 2.0 to 2.6 GeV, and  $\Delta\tau$  from 1.8 to 4.0  $\text{GeV}^{-1}$  ( $c\Delta\tau$  from 0.35 to 0.79 fm). A sample of 197  $\phi(1020)$  mesons

was accumulated for the exclusive reaction of  $ep \rightarrow e'p'\phi$  with the CLAS detector in Hall B at Jefferson Lab.

(i) Taken together with the world data sample, we find a consistent picture of  $\phi$  production on the proton. Yet the scarcity of  $\phi$  data do not permit a precise quantitative description of the production process.

(ii) We observe the expected decrease of the slope  $b_\phi$  of  $d\sigma/dt'$  on the formation length  $c\Delta\tau$  below 2 fm. The rate of the  $b_\phi$  decrease is similar to that in  $\rho$  meson production, but with a lower asymptotic value. Using a simple geometric model, the data show that the interaction size of  $\phi$  mesons with a proton is smaller than for  $\rho$  mesons.

(iii) The  $\phi$  production cross section measurement adds new information at low values of  $Q^2$  and  $W$ . The cross section dependence on  $Q^2$  is qualitatively reproduced by pomeron exchange models. The cross section dependence on  $W$  as  $W^{0.2\pm 0.1}$  at  $Q^2 = 1.3 \text{ GeV}^2$  was determined by comparison to  $\phi$  production at HERA after correcting for threshold effects. This dependence is the same as observed in photoproduction.

Additional electro- and photoproduction data from CLAS are currently being analyzed and will increase the overall qualitative and quantitative understanding of the physics that underlies vector meson production.

## ACKNOWLEDGMENTS

We would like to acknowledge the efforts of the Accelerator, the Physics Division, and the Hall B technical staff that made this experiment possible. This work was supported in part by the U.S. Department of Energy, including DOE Contract #DE-AC05-84ER40150, the National Science Foundation, the French Commissariat à l'Energie Atomique, the Italian Istituto Nazionale di Fisica Nucleare, and the Korea Science Engineering Foundation. We would also like to acknowledge useful discussions with D. Cassel, M. Pichowsky and B. Z. Kopeliovich.

## APPENDIX A: NOTATION

We denote the four-momenta of the incident and scattered electron by  $p_e$  and  $p_{e'}$ , the virtual photon by  $q \equiv p_e - p_{e'}$ , and the target and recoil proton by  $p_p$  and  $p_{p'}$ . Each four-vector can be written as  $(E, \vec{p})$  with appropriate subscripts. We use the common notation for Lorentz

invariants:  $Q^2 = -q^2 > 0$ ,  $\nu = q \cdot p_p/M_p$  ( $M_p$  is the mass of the proton), the squared hadronic center-of-mass energy  $W^2 = (q + p_p)^2$ , and  $t = (p_p - p_{p'})^2$  is the four-momentum transfer to the target. The above-threshold momentum transfer is given by  $t' = t - t_{min}(Q^2, W) < 0$ , where  $-t_{min}$  is the minimum value of  $-t$  for fixed kinematics.

## APPENDIX B: GEOMETRIC MODEL

We describe a qualitative picture of vector meson diffractive scattering within a simple geometric model. A sketch of the process is shown in Fig. 14. The virtual photon is converted into the virtual vector meson (of radius  $r_V$ ), which diffractively interacts with the proton (of radius  $r_h$ ) during a formation time  $\Delta\tau$ . Differential elastic cross sections are closely related to the charge form factors  $F(t)$  of colliding hadrons at high energy [29,45]. For small values of  $t$ , the form factors are related to the charge radii  $\langle r^2 \rangle$ , via

$$F(t) = 1 + \frac{1}{6} \langle r^2 \rangle t + O(t^2). \quad (\text{B1})$$

For hadron-hadron elastic scattering [29], the cross sections depend exponentially on  $t$ :

$$\frac{d\sigma/dt}{(d\sigma/dt)_{t=0}} = e^{bt}. \quad (\text{B2})$$

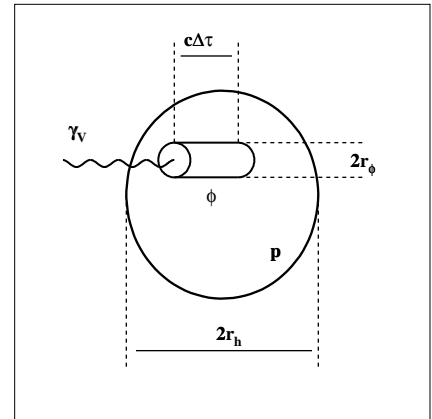


FIG. 14. Space-time picture of the  $\gamma_V p$  scattering through the conversion of the virtual photon into the virtual  $\phi$  meson inside the target proton.

Comparison of equations B1 and B2, and noting that the cross section is proportional to the square of the form factor, leads to a relationship between the radius of interaction,  $R_V^{int}$ , and the  $t$ -slope parameter  $b$ :

$$b = \frac{1}{3} (R_V^{int})^2. \quad (\text{B3})$$

The radius of interaction can be written as

$$(R_V^{int})^2 \propto \langle r_h^2 \rangle + \langle r_V^2(Q^2) \rangle, \quad (\text{B4})$$

where  $r_h$  and  $r_V$  are the radii of the nucleon and vector meson, respectively.

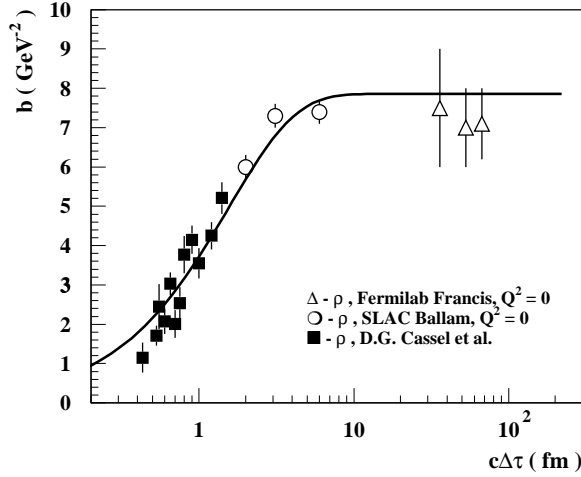


FIG. 15. The  $t$ -slope parameter dependence on  $c\Delta\tau$  for selected photo- and electroproduction data of  $\rho$  mesons. The data show a clear decrease of  $b$  with decreasing  $c\Delta\tau$  below 2 fm. The curve is a fit to Eq. B5. The photoproduction data SLAC Ballam are from Ref. [38] and Fermilab Francis from Ref. [46]. The electroproduction data CORNELL Cassel are from Ref. [15].

Because of the virtuality of the vector meson, the interaction region should also decrease if the formation distance is less than the size of the nucleon ( $c\Delta\tau \lesssim 2r_h \approx 2$  fm). A representative sample of the large body of  $\rho$  data shown in Fig. 15 suggests the following phenomenological parameterization for the  $t$ -slope dependence on  $c\Delta\tau$ :

$$b(c\Delta\tau) = \frac{1}{3} (1 - e^{-c\Delta\tau/2r_h}) (R_V^{int})^2. \quad (\text{B5})$$

A two-parameter fit to Eq. B5, ignoring any explicit dependence of  $r_\rho$  on  $Q^2$ , yields

$$b_\rho(c\Delta\tau) = (7.86 \pm 0.26) \left[ 1 - e^{-c\Delta\tau/2(0.78 \pm 0.05)} \right] \quad (\text{B6})$$

with  $\chi^2/DF = 2.08$ .

However, Eq. B5 also has an indirect dependence on  $Q^2$  through  $c\Delta\tau$ . At fixed  $W$ , we can write Eq. 1 as

$$c\Delta\tau = \frac{c(W^2 - M_p^2 + Q^2)}{M_p(Q^2 + M_\rho^2)} \quad (\text{B7})$$

Thus, we can plot Eq. B5 as a function of  $Q^2$ , using this expression for  $c\Delta\tau$ . This is shown in Fig. 16 for  $\rho$  data at the fixed value of  $W = 2.6$  GeV [15]. Thus, we see that most, if not all, of the variation of the slope parameter  $b$  can be accounted for by changes in the fluctuation time.

For the kinematics of this experiment,  $c\Delta\tau$  ( $\approx 0.5$  fm) is small compared to the size of the nucleon, so we expect the fluctuation time factor to be significant for our  $\phi$  data.

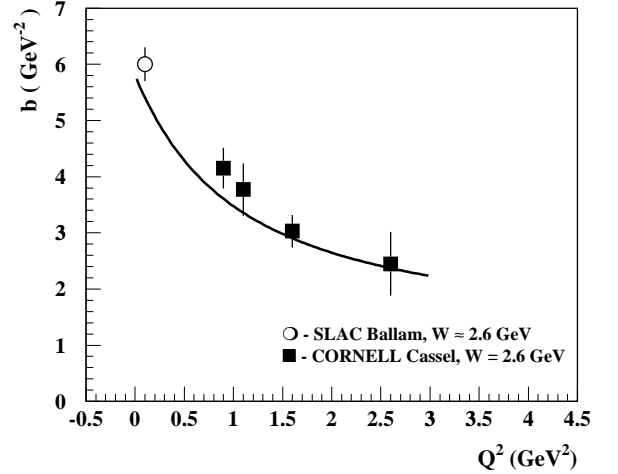


FIG. 16. The  $t$ -slope parameter dependence on  $Q^2$  for the photo- and electroproduction of  $\rho$  mesons at  $W = 2.6$  GeV. The data show a clear decrease of  $b$  with increasing  $Q^2$ . The curve is a fit to Eq. B5. The photoproduction data SLAC Ballam are from Ref. [38]. The electroproduction data CORNELL Cassel are from Ref. [15].

- 
- [1] T.H. Bauer *et al.*, Rev. Mod. Phys. **50**, 261 (1978).
  - [2] P.G.O. Freund, Nuovo Cimento **A48**, 541 (1967).
  - [3] V. Barger and D. Cline, Phys. Rev. Lett. **24**, 1313 (1970).
  - [4] H. Joos, Phys. Lett. B **24**, 103 (1967).
  - [5] K. Kajantie and J.S. Trefil, Phys. Lett. B **24**, 106 (1967).
  - [6] A. Donnachie and P.V. Landshoff, Nucl. Phys. **B244**, 322 (1984).
  - [7] A. Donnachie and P.V. Landshoff, Phys. Lett. B **185**, 403 (1987).
  - [8] M.A. Pichowsky and T.-S. H. Lee, Phys. Rev. D **56**, 1644 (1997).
  - [9] J.-M. Laget, Phys. Rev. Lett. **85**, 4682 (2000).
  - [10] Calculations based on J.-M. Laget and R. Mendez-Galain, Nucl. Phys. **A581**, 397 (1995).

- [11] CLAS Collaboration, E. Anciant *et al.*, Phys. Rev. Lett., **85**, 4682 (2000).
- [12] L.L. Frankfurt, G.A. Miller, and M.I. Strikman, Annu. Rev. Nucl. Sci. **44**, 501 (1994).
- [13] M. Vanderhaeghen, P.A.M. Guichon, and M. Guidal, Phys. Rev. D **56**, 2982 (1997).
- [14] H.W. Wang and P. Kroll, hep-ph/0005318, May 30, 2000.
- [15] D.G. Cassel *et al.*, Phys. Rev. D **24**, 2787 (1981).
- [16] HERMES Collaboration, K. Ackerstaff *et al.*, Phys. Rev. Lett. **82**, 3025 (1999).
- [17] R. Dixon *et al.*, Phys. Rev. Lett. **39**, 516 (1977).
- [18] R. Dixon *et al.*, Phys. Rev. D **19**, 3185 (1979).
- [19] W.K. Brooks, Nucl. Phys. **A663-664**, 1077 (2000).
- [20] B. Mecking *et al.*, “The CLAS Detector”, in preparation.
- [21] M. Amarian *et al.*, “The CLAS Forward Electromagnetic Calorimeter”, submitted to Nucl. Inst. and Meth., (2000).
- [22] G. Adams *et al.*, “The CLAS Cerenkov Detector”, submitted to Nucl. Inst. and Meth., (2000).
- [23] M.D. Mestayer *et al.*, Nucl. Inst. and Meth. A **449**, 81 (2000).
- [24] E.S. Smith *et al.*, Nucl. Inst. and Meth. A **432**, 265 (1999).
- [25] K. Loukachine, “Electroproduction of the  $\phi(1020)$  Vector Meson at 4 GeV,” Ph.D. thesis, Virginia Polytechnic Institute and State University, February 2000.
- [26] S.J. Taylor, “Radiative Decays of Low-Lying Excited-State Hyperons,” Ph.D. Thesis, Rice University, May 2000.
- [27] D.E. Groom *et al.*, Particle Data Group, Eur. Phys. J. C **15**, 1 (2000).
- [28] R. Ent *et al.*, “Radiative Corrections for (e,e’p) Reactions”, submitted to Phys. Rev. C.
- [29] K. Goulianos, Phys. Rep. **101**, 169 (1983).
- [30] R. Castaldi and G. Sanguinetti, Ann. Rev. Nucl. Part. Sci. **35**, 351 (1985).
- [31] T. Auger, “Photoproduction of Vector Mesons: First Results With CLAS”, Ph.D. thesis, Université de Paris, March 1999.
- [32] R. Thompson, “Eta Electroproduction in the Region of the Isospin One Half, Spin One Half 1535 MeV Baryon Resonance,” Ph.D. thesis, University of Pittsburgh, March 2000.
- [33] M. Arneodo *et al.*, Nucl. Phys. **B429**, 503 (1994).
- [34] H1 Collaboration, C. Adloff *et al.*, Phys. Lett. B **483**, 360 (2000).
- [35] ZEUS Collaboration, M. Derrick *et al.*, Phys. Lett. B **380**, 220 (1996).
- [36] ZEUS Collaboration, M. Derrick *et al.*, Phys. Lett. B **377**, 259 (1996).
- [37] H. J. Besch *et al.*, Nucl. Phys. **B70**, 257 (1974).
- [38] J. Ballam *et al.*, Phys. Rev. D **5**, 545 (1972) and J. Ballam *et al.*, Phys. Rev. D **7**, 3150 (1973).
- [39] S.J. Brodsky *et al.*, Phys. Rev. D **50**, 3134 (1994).
- [40] EMC Collaboration, J.J. Aubert *et al.*, Phys. Lett. B **161**, 203 (1985).
- [41] B. Naroska, hep-ex/0006010 (2000).
- [42] H.-J. Behrend *et al.*, Nucl. Phys. **B144**, 22 (1978).
- [43] L. Frankfurt, W. Koepf, and M. Strikman, Phys. Rev. D **54**, 3194 (1996).
- [44] B.Z. Kopeliovich *et al.*, Phys. Lett. B **309**, 179 (1993).
- [45] B. Povh, hep-ph/9806379, Jun 16, 1998, and references therein.
- [46] W. Francis *et al.*, Phys. Rev. Lett. **38**, 633 (1977).